Pergamon

Int. J. Heat Mass Transfer. Vol. 40, No. 2, pp. 379–392, 1997

0017–9310/97 $15.00+0.00

PII: S0017–9310(96)00095–6

Transient thermal convection in a spherical enclosure containing a fluid core and a porous shell

HOA D. NGUYEN and SEUNGHO PAIK
Idaho National Engineering Laboratory, Idaho Falls, ID 83415, U.S.A.

and

IOAN POP
Faculty of Mathematics, University of Cluj, R-3400 Cluj, Romania

(*Received* 2 *March* 1995 *and in final form* 1 *March* 1996)

Abstract—Transient natural convection in a spherical enclosure containing a central core fluid and a porous shell fully saturated with the same fluid is investigated numerically. Simulations are based on a mathematical model consisting of the Navier–Stokes equations for the fluid region, the Brinkman equation for flow through porous media, a convective diffusion equation for energy transport, and the Boussinesq approximation for buoyancy. Solutions are obtained by a hybrid spectral method which combines the concepts of Galerkin and collocation methods with Legendre and Chebyshev polynomials employed as basis functions, respectively. Time advancement is accomplished by a combined Adams–Bashforth and backward Euler schemes. The numerical results exhibit remarkable effects along the porous–fluids interface; however, the overall heat flux is only sensitive to the thermal conductivity ratio of the solid matrix to the fluid.

1. INTRODUCTION

Buoyancy-generated convection in enclosures composed of simultaneous fluid and fluid-saturated porous layers has recently become a topic of great interest owing to the numerous applications. Representative examples include the transport in geologic formations associated with nuclear waste repositories and in geothermal systems, processing of metal alloys, the optimal usage of thermal insulation and reservoir engineering. Clearly, there is a need for a fundamental understanding of the transport processes associated with systems containing a fluid–porous interface. In this paper, our effort will be directed toward natural convection in a spherical enclosure in which the central fluid core is surrounded by a porous layer saturated with the same fluid. To the authors' knowledge, this scenario has not been investigated.

Despite the interdisciplinary nature of the problem, very little research has been conducted to explore the transport phenomena in fluid–porous composite systems. One of the early theoretical analyses in this area, with particular attention to geophysical systems, has been the work of Nield [1] who studied the onset of convection in a fluid layer lying on top of a porous layer subjected to uniform heating at the bottom. The same physical setting, but with heating from a side, was considered by Nishimura *et al.* [2], both experimentally and numerically using a finite element method. Their comparisons between the simulated results and the measured data indicated a good agreement. However, because the range of their experimental conditions was limited to conduction-dominated heat transfer in the porous medium, only such cases were examined. In a different context, this type of problem also arose in thermal insulation engineering and was treated by Tong and his associates [3–5]. The main feature that differentiates their work from the aforementioned study is the layers' orientation which was arranged in such a way as to be parallel with the direction of gravity in an effort to evaluate the thermal performance of partially filled insulation systems. Their results are quite surprising because they exhibit the fact, though somewhat contradictory to common sense, that filling the entire enclosure with a porous material is not necessarily a prerequisite for an effective suppression of convective heat transfer. That is, there exists a certain thickness at which further filling of the insulation does not lead to any lower heat transfer rate. Until recently, this problem has emerged in material processing where extended freezing temperature ranges of alloys creates, in addition to the liquid and solid phases, a mushy region that acts like a porous material, at least at the microscopic level. Beckermann *et al.* [6, 7] have formulated the problem to include the effects of quadratic drag and viscous diffusion. For a more specialized account in this area, the article by Voller *et al.* [8] and the references therein should be consulted.

In the work reviewed thus far, the physical domain

NOMENCLATURE

c	specific heat at constant pressure of the fluid	Δt	time increment
c_s	heat capacity of the solid phase	θ	angular coordinate
Da	Darcy number	Θ	temperature
$\mathbf{k}$	unit vector in the vertical direction	κ	thermal conductivity of the solid porous material
K	intrinsic permeability of the porous medium	$\hat{\kappa}$	overall thermal conductivity of the fluid saturate porous medium
NL	number of Legendre modes	μ	viscosity
Nu	Nusselt number	ξ	transformed radial coordinate
p	pressure	ρ	density
Pr	Prandtl number	ϕ	porosity
r	radial coordinate	Φ	property ratio of the fluid to the porous material
R	sphere radius	ψ	stream function.
Ra	Rayleigh number		
t	time		
$\mathbf{u}$	dimensionless velocity vector.	Subscripts	
		f	fluid–porous medium interface
Greek symbols		s	solid porous material
α	thermal diffusivity	w	wall condition
β	thermal expansion of the fluid	0	initial condition.

of the problem has been rectangular. Under certain circumstances, the problem may be inherently spherical and therefore it may be better solved in spherical coordinates. From this standpoint, the objectives of this paper are to establish a mathematical formalism as well as a solution procedure to deal with this type of problem, and at the same time to uncover the essential physics of the convective flow phenomena in a combined fluid and porous layering spherical enclosure. Because the gravity components appear in both r- and θ-direction, the flow structure will correspondingly be different from that previously reported. In addition, the motion within the fluid core will now be dictated by the thermal and momentum transport in the porous layer. One unique feature of the present study is the transient behaviors of the system in which the motion ceases to exist when the interior fluid becomes in thermal equilibrium with the surrounding wall. Similar physical systems have been investigated wherein the spherical enclosure is completely as opposed to partially, filled with a fluid (see, for example, Shen *et al.* [9]).

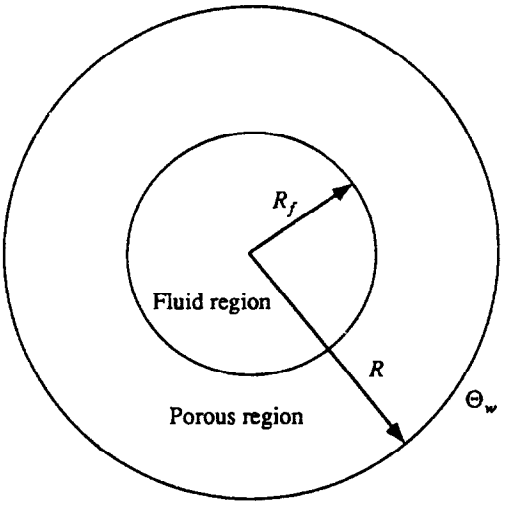

Fig. 1. Schematic of the physical system.

2. FORMULATION

2.1. *Problem statement*

Shown in Fig. 1 is a schematic of a spherical enclosure of radius R, consisting of a fluid core of radius R_f surrounded by a fluid-saturated porous layer of thickness $(R-R_f)$. Initially, the entire sphere is kept at temperature Θ_0. Suddenly, it is brought into contact with the surroundings such that the surface temperature is always maintained at Θ_w, presumably greater than Θ_0. Because of the imposed thermal gradient, heat penetrates into the sphere interior to cause a nonuniformity in density, which then derives the flow. From our knowledge of transport processes, the induced motion is weak during the early stage and conduction will dominate the heat transfer. As time elapses, the flow is expected to be more intensified and could play a leading role in later periods as buoyancy overcomes the viscous resistance.

Predicting the evolution of the flow and temperature fields necessitates a simultaneous solution of a set of equations derivable from the laws of conservation of mass, momentum and energy. Unfortunately, these equations are more often than not too difficult, if not intractable, to solve unless sim-

plifications are made. Considering these complexities, we shall adopt the following assumptions: (i) internal thermal resistance is relatively large so that the heat transfer outside the enclosure can be neglected, (ii) the Boussinesq approximations are valid and that gravity acts in the horizontal direction; hence, the problem is symmetrical about the horizontal axis, (iii) the porous layer is homogeneous and isotropic and that the flow conforms to the Brinkman model, an extension to the Darcian regime to take into account boundary effects. Since inertia was not considered in his model, it is not valid for high permeability materials, (iv) the fluid and the solid matrix within the porous medium are in local thermal equilibrium, which is justifiable on the basis of the enormous interfacial area between the fluid and the solid, (v) thermal dispersion due to interpore mixing is negligible compared to diffusion unless the velocity is sufficiently large, and (vi) the process is two-dimensional in r and θ, as commonly assumed in the past [9].

2.2. *Mathematical formulation*

With the assumptions stated in the foregoing subsection, the mass, momentum and energy conservation laws can be expressed in nondimensional form as

$$\nabla \cdot \mathbf{u} = 0, \tag{1}$$

$$\frac{\partial u}{\partial t} + \mathbf{u} \cdot \nabla \mathbf{u} = -\nabla p + Pr \nabla^2 \mathbf{u} + RaPr\Theta \mathbf{k}, \tag{2}$$

$$\frac{\partial \Theta}{\partial t} + \mathbf{u} \cdot \nabla^2 \Theta = \nabla^2 \Theta \tag{3}$$

for the fluid region in the core, and

$$\nabla \cdot \hat{\mathbf{u}} = 0, \tag{4}$$

$$\frac{\partial \hat{\mathbf{u}}}{\partial t} = -\nabla^2 p + Pr \nabla^2 \hat{\mathbf{u}} + RaPr\hat{\Theta}\mathbf{k} - \frac{Pr}{Da}\hat{\mathbf{u}}, \tag{5}$$

$$\Phi_c \frac{\partial \hat{\Theta}}{\partial t} + \hat{\mathbf{u}} \cdot \nabla \hat{\Theta} = \Phi_\kappa \nabla^2 \hat{\Theta} \tag{6}$$

for the porous shell. Note that a hat has been used to denote the porous region.

In the above equations, all the variables have been made dimensionless according to the following definitions:

$$\left.\begin{aligned} r^* &= \frac{r}{R} \quad t^* = \frac{t\alpha}{R^2} \quad \mathbf{u}^* = \frac{\mathbf{u}R}{\alpha} \\ p^* &= \frac{pR^2}{\rho\alpha^2} \quad \Phi_c = \phi + (1-\phi)\frac{\rho_s - c_s}{\rho_0 c} \\ \Phi_\kappa &= \frac{\hat{\kappa}}{\kappa} \quad \Theta^* = \frac{\Theta - \Theta_0}{\Theta_w - \Theta_0} \\ Ra &= \frac{\rho g \beta (\Theta_w - \Theta_0) R^3}{\mu\alpha} \quad Da = \frac{K}{R^2} \quad Pr = \frac{c\mu}{\kappa} \end{aligned}\right\} \tag{7}$$

in which all the parameters are defined in the Nomenclature. For convenience, asterisks have been omitted in equations (1)–(6).

The initial and boundary conditions to be satisfied by equations (1)–(6) are given as

(i) At $t = 0$

$$\mathbf{u} = \hat{\mathbf{u}} = 0 \quad \text{and} \quad \Theta = \hat{\Theta} = 0. \tag{8}$$

(ii) At the surface ($r = 1$)

$$\hat{\mathbf{u}} = 0 \quad \text{and} \quad \hat{\Theta} = 1. \tag{9}$$

(iii) At the interface ($r = r_i$)

$$\left.\begin{aligned} &\mathbf{u} = \hat{\mathbf{u}} \quad p = \hat{p} \\ &r\frac{\partial}{\partial r}\left(\frac{u_\theta}{r}\right) + \frac{1}{r}\frac{\partial u_r}{\partial \theta} = r\frac{\partial}{\partial r}\left(\frac{\hat{u}_\theta}{r}\right) + \frac{1}{r}\frac{\partial \hat{u}_r}{\partial \theta}, \\ &\Theta = \hat{\Theta} \quad \kappa\frac{\partial \Theta}{\partial r} = \hat{\kappa}\frac{\partial \hat{\Theta}}{\partial r} \end{aligned}\right\} \tag{10}$$

(iv) At the center ($r = 0$)

$$\mathbf{u} \text{ and } \Theta \text{ are finite.} \tag{11}$$

Under the axisymmetric conditions, the problem is two-dimensional and the vorticity is a scalar quantity. To take advantage of these facts, it is a common practice to apply a curl to the momentum equations (2) and (5) to eliminate the pressure, and the resulting equations are then simplified to desired forms using appropriate vector identities. Thus,

$$\frac{1}{\sin\theta} D^2 \left[D^2 - \frac{1}{Pr}\frac{\partial}{\partial t} \right] \psi + \frac{1}{Pr} J(\psi, D^2\psi / r^2 \sin^2\theta) = -Ra\left[r\sin\theta \frac{\partial \Theta}{\partial r} + \cos\theta \frac{\partial \Theta}{\partial \theta} \right], \tag{12}$$

$$\frac{\partial \Theta}{\partial t} - \frac{1}{r^2 \sin\theta} J(\psi, \Theta) = \nabla^2 \Theta, \tag{13}$$

and

$$\frac{1}{\sin\theta} D^2 \left[D^2 - \left(\frac{1}{Da} + \frac{1}{Pr}\frac{\partial}{\partial t} \right) \right] \hat{\psi} = -Ra\left[r\sin\theta \frac{\partial \hat{\Theta}}{\partial r} + \cos\theta \frac{\partial \hat{\Theta}}{\partial \theta} \right], \tag{14}$$

$$\Phi_c \frac{\partial \hat{\Theta}}{\partial t} - \frac{1}{r^2 \sin\theta} J(\hat{\psi}, \hat{\Theta}) = \Phi_\kappa \nabla^2 \hat{\Theta}, \tag{15}$$

where ψ is the stream function defined in such a way to automatically satisfy the incompressibility constraint. That is,

$$(\mathbf{u}, \hat{\mathbf{u}}) = \frac{\mathbf{e}_r}{r^2 \sin\theta}\frac{\partial(\psi, \hat{\psi})}{\partial \theta} - \frac{\mathbf{e}_\theta}{r\sin\theta}\frac{\partial(\psi, \hat{\psi})}{\partial r}. \tag{16}$$

The operators introduced in equations (12)–(15) are given by

$$J(\psi, \Theta) \equiv \frac{\partial \psi}{\partial r}\frac{\partial \Theta}{\partial \bar{\mu}} - \frac{\partial \Theta}{\partial r}\frac{\partial \psi}{\partial \bar{\mu}}, \tag{17a}$$

$$D^2 \equiv \frac{\partial^2}{\partial r^2} + \frac{(1-\bar{\mu}^2)}{r^2}\frac{\partial^2}{\partial \bar{\mu}^2}, \tag{17b}$$

$$\nabla^2 \equiv \frac{1}{r^2}\frac{\partial}{\partial r}\left(r^2\frac{\partial}{\partial r}\right) + \frac{1}{r^2}\frac{\partial}{\partial \bar{\mu}}\left[(1-\bar{\mu}^2)\frac{\partial}{\partial \bar{\mu}}\right], \tag{17c}$$

with $\bar{\mu} = \cos\theta$. One of the main advantages offered by this approach is the elimination of the difficulty associated with the lack of boundary conditions for the pressure in the velocity–pressure formulation and for the vorticity in the vorticity–stream function formulation.

3. SOLUTION METHODOLOGIES

In this section we shall describe a numerical scheme, first-order accurate in time and spectrally accurate in space, which decouples the equations from interactions between the flow and energy and between the fluid and the porous regions. This is achieved by using a combination of techniques as detailed below.

3.1. *Time discretization*

In this approach, the momentum–energy couplings are removed by integrating the convection terms explicitly and the diffusion terms implicitly using the Adams–Bashforth and the backward Euler schemes, respectively. In doing so equations (12)–(15) become

$$\begin{aligned}\frac{1}{\sin\theta}D^2\left[D^2 - \frac{1}{Pr\Delta t}\right]\psi^{m+1} &= -\left(\frac{1}{Pr\Delta t}\right)\frac{1}{\sin\theta}D^2\psi^m \\ &\quad - \frac{1}{2Pr}[3J(\psi^m, D^2\psi^m/r^2\sin^2\theta) \\ &\quad - J(\psi^{m-1}, D^2\psi^{m-1}/r^2\sin^2\theta)] \\ &\quad + \frac{Ra}{2}\left[3\left(r\sin\theta\frac{\partial\Theta^m}{\partial r} + \cos\theta\frac{\partial\Theta^m}{\partial\theta}\right)\right. \\ &\quad \left. - \left(r\sin\theta\frac{\partial\Theta^{m-1}}{\partial r} + \cos\theta\frac{\partial\Theta^{m-1}}{\partial\theta}\right)\right],\end{aligned} \tag{18}$$

$$\left(\frac{1}{\Delta t} - \nabla^2\right)\Theta^{m+1} = \frac{1}{\Delta t}\Theta^m + \frac{1}{2r^2\sin\theta} \times [3J(\psi^m, \Theta^m) - J(\psi^{m-1}, \Theta^{m-1})], \tag{19}$$

$$\begin{aligned}\frac{1}{\sin\theta}D^2\left[D^2 - \left(\frac{1}{Da} + \frac{1}{Pr\Delta t}\right)\right]\hat{\psi}^{m+1} &= -\left(\frac{1}{Pr\Delta t}\right)\frac{1}{\sin\theta}D^2\hat{\psi}^m \\ &\quad + \frac{Ra}{2}\left[3\left(r\sin\theta\frac{\partial\hat{\Theta}^m}{\partial r} + \cos\theta\frac{\partial\hat{\Theta}^m}{\partial\theta}\right)\right. \\ &\quad \left. - \left(r\sin\theta\frac{\partial\hat{\Theta}^{m-1}}{\partial r} + \cos\theta\frac{\partial\hat{\Theta}^{m-1}}{\partial\theta}\right)\right],\end{aligned} \tag{20}$$

$$\left(\frac{\Phi_c}{\Delta t} - \Phi_\kappa\nabla^2\right)\hat{\Theta}^{m+1} = \frac{\Phi_c}{\Delta t}\hat{\Theta}^m + \frac{1}{2r^2\sin\theta} \times [3J(\hat{\psi}^m, \hat{\Theta}^m) - J(\hat{\psi}^{m-1}, \hat{\Theta}^{m-1})], \tag{21}$$

where Δt is the time increment and the superscript m denotes the time level. Since the truncation error associated with the Adams–Bashforth formula is on the order of $(\Delta t)^2$ while the backward Euler is Δt, the overall accuracy of the integration scheme is first-order with respect to time.

3.2. *Spectral methods*

Following the series truncation procedure [10, 11], the stream function and temperature are expanded as

$$\begin{Bmatrix}\psi^m \\ \hat{\psi}^m\end{Bmatrix} = \sum_{n=1}^{NL}\begin{Bmatrix}\psi_n^m \\ \hat{\psi}_n^m\end{Bmatrix}\int_{\bar{\mu}}^{1} P_n(\bar{\mu})\,d\bar{\mu}, \tag{22a}$$

$$\begin{Bmatrix}r\Theta^m \\ r\hat{\Theta}^m\end{Bmatrix} = \sum_{n=0}^{NL}\begin{Bmatrix}\Theta_n^m \\ \hat{\Theta}_n^m\end{Bmatrix}P_n(\bar{\mu}), \tag{22b}$$

where $P_n(\bar{\mu})$ is the Legendre polynomial of order n with $\bar{\mu} = \cos\theta$. It should be pointed out that we have expanded $r\Theta$ instead of Θ alone, since it enables us to resolve the temperature boundary condition which would otherwise be indefinite at the center of the sphere.

Upon substituting these series into equations (18)–(21) and after much algebraic manipulation, there results

$$\begin{aligned}\frac{1}{n(n+1)}\frac{d^4\psi_n^{m+1}}{dr^4} - \left[\frac{2}{r^2} + \frac{1}{n(n+1)Pr\Delta t}\right]\frac{d^2\psi_n^{m+1}}{dr^2} \\ + \frac{4}{r^3}\frac{d\psi_n^{m+1}}{dr} + \left[\frac{(n+3)(n-2)}{r^2} + \frac{1}{Pr\Delta t}\right]\frac{\psi_n^{m+1}}{r^2} \\ = S_i(0,1,\psi,\Theta),\end{aligned} \tag{23}$$

$$\frac{d^2\Theta_n^{m+1}}{dr^2} - \left[\frac{n(n+1)}{r^2} + \frac{1}{\Delta t}\right]\Theta_n^{m+1} = H_n(1,1,\psi,\Theta), \tag{24}$$

$$\begin{aligned}\frac{1}{n(n+1)}\frac{d^4\hat{\psi}_n^{m+1}}{dr^4} - \left[\frac{2}{r^2} + \frac{1}{n(n+1)}\left(\frac{1}{Da} + \frac{1}{Pr\Delta t}\right)\right] \\ \times\frac{d^2\psi_n^{m+1}}{dr^2} + \frac{4}{r^3}\frac{d\hat{\psi}_n^{m+1}}{dr} + \left[\frac{(n+3)(n-2)}{r^2}\right. \\ \left. + \left(\frac{1}{Da} + \frac{1}{Pr\Delta t}\right)\right]\frac{\hat{\psi}_n^{m+1}}{r^2} = S_n(1,0,\hat{\psi},\hat{\Theta}),\end{aligned} \tag{25}$$

$$\begin{aligned}\frac{d^2\hat{\Theta}_n^{m+1}}{dr^2} - \left[\frac{n(n+1)}{r^2} + \frac{\Phi_c}{\Phi_\kappa\Delta t}\right]\hat{\Theta}_n^{m+1} \\ = H_n(\Phi_c, \Phi_\kappa, \hat{\psi}, \hat{\Theta}),\end{aligned} \tag{26}$$

which are ordinary differential equations since the angular dependences have been eliminated. Note that

the right-hand-sides in these equations have been abbreviated by S_n and H_n as defined in the Appendix.

Numerous techniques exist for transforming the above equations into their corresponding discrete analogues. Among them, the Chebyschev pseudospectral method seems to be quite appropriate because of its properties being very similar to those of the spectral Galerkin method and is thus adopted here. More importantly, the use of this method in conjunction with the Gauss–Lobatto quadrature set of abscissas as the collocation points satisfies our need of an adequate computational grid to resolve the potential stiff gradients at the surface. Since this method has been described at length in the literature (see Nguyen and Chung [11], for instance), details are omitted.

3.3. *Influence matrix technique*

Although the flow and the energy equations are no longer coupled, the interactions between the fluid and the porous shell at the interface require the solution to be obtained either simultaneous or iterative. Due to this complication, we shall apply an influence matrix technique to further decouple them. In this manner, the solutions are sought as linear combinations of auxiliary problems of the form [10]

$$\begin{Bmatrix} \psi_n^{m+1} \\ \hat{\psi}_n^{m+1} \end{Bmatrix} = \begin{Bmatrix} \Psi_0 \\ \hat{\Psi}_0 \end{Bmatrix} + a_1 \begin{Bmatrix} \Psi_1 \\ 0 \end{Bmatrix} + a_2 \begin{Bmatrix} \Psi_2 \\ 0 \end{Bmatrix} + a_3 \begin{Bmatrix} 0 \\ \hat{\Psi}_1 \end{Bmatrix} + a_4 \begin{Bmatrix} 0 \\ \hat{\Psi}_2 \end{Bmatrix}, \quad (27a)$$

$$\begin{Bmatrix} \Theta_n^{m+1} \\ \hat{\Theta}_n^{m+1} \end{Bmatrix} = \begin{Bmatrix} \Xi_0 \\ \hat{\Xi}_0 \end{Bmatrix} + b_1 \begin{Bmatrix} \Xi_1 \\ 0 \end{Bmatrix} + b_2 \begin{Bmatrix} 0 \\ \hat{\Xi}_1 \end{Bmatrix}, \quad (27b)$$

where $a_1 \ldots, a_4$, b_1 and b_2 are coefficients to be determined from the fluid–porous interface couplings. Upon imposing these constraints, there results two systems of equations:

$$\begin{bmatrix} \Psi_1 & \Psi_2 & -\hat{\Psi}_1 & -\hat{\Psi}_2 \\ \Psi_1' & \Psi_2' & -\hat{\Psi}_1' & -\hat{\Psi}_2' \\ \Psi_1'' & \Psi_2'' & -\hat{\Psi}_1'' & -\hat{\Psi}_2'' \\ \Psi_1''' & \Psi_2''' & -\hat{\Psi}_1''' & -\hat{\Psi}_2''' \end{bmatrix} \begin{Bmatrix} a_1 \\ a_2 \\ a_3 \\ a_4 \end{Bmatrix} = \begin{Bmatrix} \hat{\Psi}_0 - \Psi_0 \\ \hat{\Psi}_0' - \Psi_0' \\ \hat{\Psi}_0'' - \Psi_0'' \\ \hat{\Psi}_0''' - \Psi_0''' \end{Bmatrix}, \quad (28)$$

$$\begin{bmatrix} \Xi_1 & -\hat{\Xi}_1 \\ r_f\Xi_1' - \Xi_1 & -\Phi_\kappa(r_f\hat{\Xi}_1' - \hat{\Xi}_1) \end{bmatrix} \begin{Bmatrix} b_1 \\ b_2 \end{Bmatrix} = \begin{Bmatrix} \hat{\Xi}_0 - \Xi_0 \\ \Phi_\kappa(r_f\hat{\Xi}_0' - \hat{\Xi}_0) - (r_f\Xi_0' - \Xi_0) \end{Bmatrix}, \quad (29)$$

in which the primes denote derivative with respect to r. The auxiliary functions are required to be the solution of the following simple, but related, problems:

$$\begin{cases} \dfrac{1}{n(n+1)}\Psi_l^{iv} - \left[\dfrac{2}{r^2} + \dfrac{1}{n(n+1)Pr\Delta t}\right]\Psi_l'' \\ \quad + \dfrac{4}{r^3}\Psi_l' + \left[\dfrac{(n+3)(n-2)}{r^2} + \dfrac{1}{Pr\Delta t}\right]\dfrac{\Psi_l}{r^2} \\ \quad = \delta_{0l}S_n(0,1,\psi,\Theta), \quad l = 0,1,2 \\ \begin{cases} \Psi_0(r_f) = 0 & \Psi_0'(r_f) = 0 & \Psi_0(0) = 0 & \Psi_0'(0) = 0 \\ \Psi_1(r_f) = 1 & \Psi_1'(r_f) = 0 & \Psi_1(0) = 0 & \Psi_1'(0) = 0 \\ \Psi_2(r_f) = 0 & \Psi_2'(r_f) = 1 & \Psi_2(0) = 0 & \Psi_2'(0) = 0 \end{cases} \end{cases} \quad (30)$$

$$\begin{cases} \dfrac{1}{n(n+1)}\hat{\Psi}_l^{iv} - \left[\dfrac{2}{r^2} + \dfrac{1}{n(n+1)}\left(\dfrac{1}{Da} + \dfrac{1}{Pr\Delta t}\right)\right]\hat{\Psi}_l'' \\ \quad + \dfrac{4}{r^3}\hat{\Psi}_l' + \left[\dfrac{(n+3)(n-2)}{r^2} + \left(\dfrac{1}{Da} + \dfrac{1}{Pr\Delta t}\right)\right]\dfrac{\hat{\Psi}_l}{r^2} \\ \quad = S_n(1,0,\hat{\psi},\hat{\Theta}), \quad l = 0,1,2 \\ \begin{cases} \hat{\Psi}_0(1) = 0 & \hat{\Psi}_0'(1) = 0 & \hat{\Psi}_0(r_f) = 0 & \hat{\Psi}_0'(r_f) = 0 \\ \hat{\Psi}_1(1) = 0 & \hat{\Psi}_1'(1) = 0 & \hat{\Psi}_1(r_f) = 1 & \hat{\Psi}_1'(r_f) = 0 \\ \hat{\Psi}_2(1) = 0 & \hat{\Psi}_2'(1) = 0 & \hat{\Psi}_2(r_f) = 0 & \hat{\Psi}_2'(r_f) = 1 \end{cases} \end{cases} \quad (31)$$

$$\begin{cases} \Xi_l'' - \left[\dfrac{n(n+1)}{r^2} + \dfrac{1}{\Delta t}\right]\Xi_l = \delta_{0l}H_n(1,\psi,\Theta), \quad l = 0,1 \\ \begin{cases} \Xi_0(r_f) = 0 & \Xi_0(0) = 0 \\ \Xi_1(r_f) = 1 & \Xi_1(0) = 0 \end{cases} \end{cases} \quad (32)$$

$$\begin{cases} \hat{\Xi}_l'' - \left[\dfrac{n(n+1)}{r^2} + \dfrac{\Phi_c}{\Phi_\kappa\Delta t}\right]\hat{\Xi}_l = \delta_{0l}H_n(\Phi_\kappa,\hat{\psi},\hat{\Theta}), \\ \qquad\qquad\qquad\qquad\qquad\qquad\qquad\qquad l = 0,1, \\ \begin{cases} \hat{\Xi}_0(1) = \delta_{0n} & \hat{\Xi}_0(r_f) = 0 \\ \hat{\Xi}_1(1) = 0 & \hat{\Xi}_1(r_f) = 1 \end{cases} \end{cases} \quad (33)$$

where δ_{0l} is the Kronecker delta.

Before leaving this section, it is worthwhile to add two remarks regarding the above procedure. First, each of the auxiliary problems so constructed is self-contained and can be solved independently. Second, the introduction of the auxiliary functions does not seem to create much additional computing burden, because the nonzero components can be solved analytically and their solutions remain unchanged throughout the course of simulation. Thus, the influence matrix technique provides a means to decompose a large problem into smaller ones which are suitable for parallel computations.

4. RESULTS AND DISCUSSION

Owing to the transient nature of the problem on the one hand and the involvement of several model

Table 1. Values of simulation parameters

Parameters	Values	Parameters	Values
Ra	10^5	r_f	0.5
Da	10^{-5}	NL	10
Pr	3.0	NT†	31
Φ_κ	0.7	Δt	10^{-3}
Φ_c	1		

†Number of collocation points.

parameters on the other, a full parametric study necessitates a large number of runs. Though this type of study is possible as far as computing resources are concerned, it is prohibitive in view of the excessive space needed for presenting the results. Considering this limitation, the remainder of the discussion will be organized as follows. First, the transient behavior of the physical system is examined in an effort to provide some physical insight on how the heat transfer process evolves and to identify various stages where one mechanism dominates the others. Second, we shall consider the effects of Rayleigh number on the flow and temperature fields. Last, we shall examine the influence of other parameters on the interfacial heat flux, the interfacial temperature, and the interfacial velocity components. For the purpose of illustrations, Φ_c is set to be 1 and remains the same throughout the calculations, since its role is limited to shifting of the time scale in the porous region.

For convenience, all the graphics presented hereafter are shown only for half of the enclosure due to its symmetry. Unless otherwise noted, values of the simulation parameters are listed in Table 1, herein referred to as the base case. The number of Legendre functions and collocation points so tabulated are determined from a convergence analysis based on the mean Nusselt number, defined as

$$Nu \equiv \left(\frac{\partial \hat{\Theta}_0}{\partial r} - \hat{\Theta}_0 \right)\Bigg|_{r=1}, \tag{34}$$

and are summarized in Table 2. From those data, $NT = 21$ and $NL = 4$ would seem to be a logical choice since this set gives satisfactory Nusselt numbers, correct to two decimal places. However, care must be taken to choose a pair of values which not only warrant converged solutions in the porous medium, but are also sufficiently large to ensure that the interior solutions are adequately represented. Thus, we adopt a value of 10 for NL and 31 for NT.

Table 2. Convergence of mean Nusselt number at $t = 0.1$

	NL		
NT†	4	8	10
21	1.194696	1.194693	1.194693
31	1.192904	1.192902	1.192902
41	1.192435	1.192432	1.192432

†Number of collocation points.

Figure 2(a–c) depicts the velocity vectors and the isotherms using the above specification at three different instants ($t = 0.005$, 0.05 and 0.2) to represent the early, intermediate and late-time periods, respectively. At small times, $t = 0.005$, appreciable motion is seen to be confined in the vicinity of the sphere surface and in the fluid core. In the porous region, the flow is upward along the inner edge and downward along the outer edge and forms a closed loop similar to Hill's spherical vortex. Inside the fluid region, the influx of momentum due to flow penetration in the rear causes fluid particles there to move and eventually exit at the frontal surface. Because the flow resistance in the pore is much greater than that in the core, the velocity in the core is larger than in the porous medium. As shown in Fig. 2(a), the temperature contours exhibit a spherical symmetry about the center; hence implying condition-controlled heat transfer during this period. Careful inspection of the figure reveals that the temperature in the fluid core is practically uniform. As time progresses [see Fig. 2(b)], heat further penetrates into the fluid zone to create temperature gradients, which together with the momentum transfer at the interface lead to strong convective currents. Due to the relatively high velocity in the fluid region, the interfacial shearing force appears to enhance the flow in the porous region to a certain extent. The departure of isotherms from spherical symmetry provides evidence that convection is playing a greater role in the transport process. Such a transition is most apparent inside the fluid core where the contours were pushed toward the frontal surface to form a kidney-like shape. This trend is, to a lesser degree, also observed in the porous region with contours being farther apart than those in the front. Figure 2(c) illustrates the results at longer time, $t = 0.2$, at which the velocity has already begun diminishing. This is expected, since no flow would exist at the state of thermal equilibrium where all thermal gradients vanish to zero. Even with a weakening flow field, convection still plays a major role on the heat transfer process.

Accompanying Fig. 2 is Fig. 3(a–c) showing the temporal developments of the temperature, the Nusselt number and the velocity along the interface, respectively. For the temperature, it is practically at its initial value at small times. As soon as heat penetrated to the core fluid, a substantial temperature variation along the interface is observed as measured by the temperature difference between the two poles. Once this temperature difference reaches the maximum value, it begins to level out as the thermal equilibrium state, i.e. $\Theta = \hat{\Theta} = 1$ everywhere, is reached. In the same manner, convection is held responsible for the variations of the local Nusselt number, hence the local heat flux, along the interface. The interfacial velocity is presented in Fig. 3(c) with the solid and open symbols representing the tangential

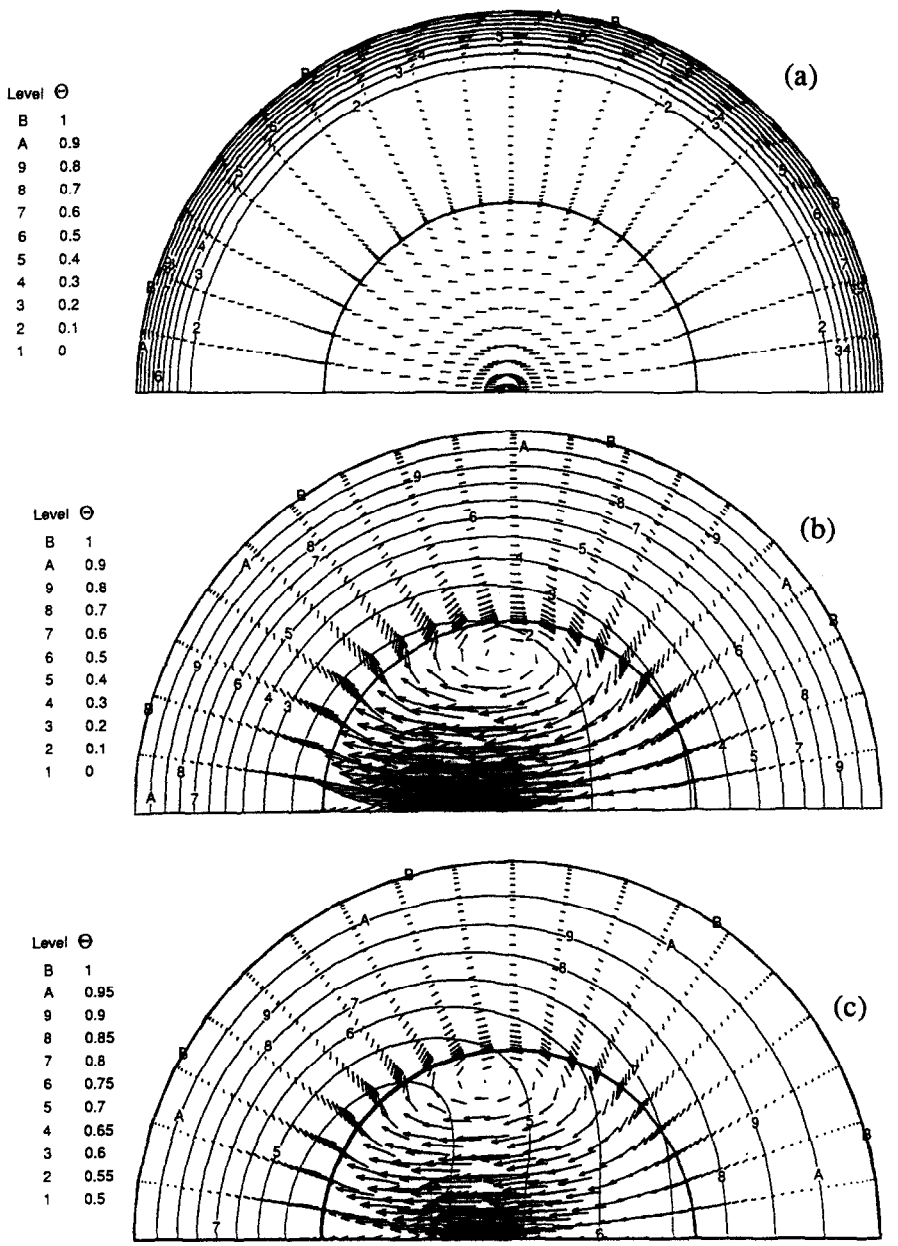

Fig. 2. Temporal development of the velocity and temperature fields for $Ra = 10^5$, $Da = 10^{-5}$, $Pr = 3$ and $\Phi_s = 0.7$: (a) $t = 0.005$; (b) $t = 0.05$; (c) $t = 0.2$.

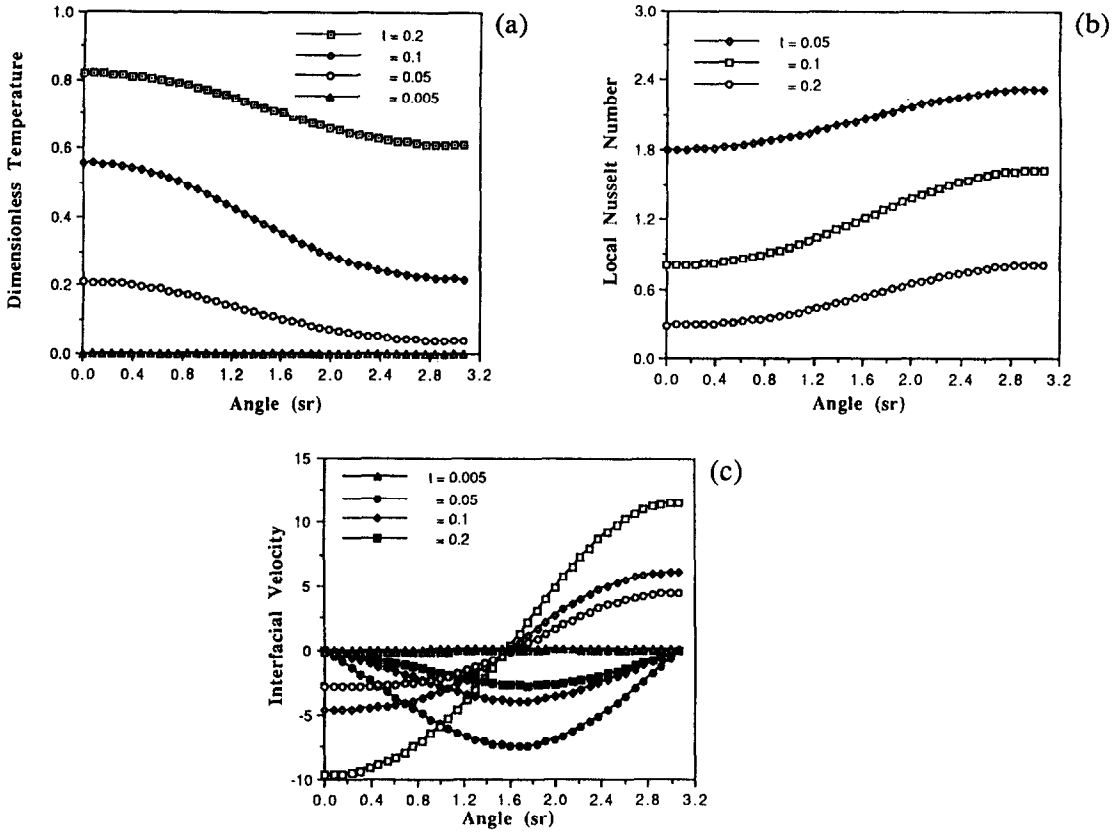

Fig. 3. Time variations of interfacial quantities: (a) temperature; (b) Nusselt number; (c) velocity components.

and radial components, respectively. One interesting note about their evolution is that u_θ appears to be established quickly and to be subsequently dying out while u_r is still in the developmental stage.

Figure 4(a–c) demonstrates the effects of the Rayleigh number on the velocity and temperature fields at $t = 0.2$. Structurally, the flows associated with $Ra = 10^4$, 10^5 and 10^6 are very much alike, except that the center of the vortex seems to be moving closer to the interface as Ra increases. Since the vectors in these three plots were drawn to scale, the steady escalation of the flow intensity is obvious, as one would anticipate. The temperature field, on the other hand, reflects the changes in the flow structure well as indicated by the spacings between isotherms and the sharp temperature gradients near the interface. A careful comparison of these figures reveals that the higher the Rayleigh number, the shorter is the time required for thermal equilibrium.

Figure 5 shows the history of Nusselt numbers of four different cases in which one parameter is altered at a time. Among the parameters being examined, Pr is clearly the least sensitive [see Fig. 5(b)] as evidenced by the collapse of the four graphs into a single curve. When Ra and Da vary, the effects are small but visible, at least for the ranges of values considered. However, one should not be mislead by the information revealed from Fig. 5(a,c), because the Nusselt numbers may differ as much as 20 and 10%, respectively. Here, it is important to note the crossing of the Nusselt number curves which could be attributed by the circulating motion inside the enclosure. This aspect is common in heat transfer associated with a liquid droplet [12]. In Fig. 5(d), significant effects occur as the ratio of the thermal conductivity increases from 0.3 to 5. This can be explained by the fact that the thermal conductance of the outer medium is higher than that of the interior, leading to a higher fraction of energy accumulated in the exterior, thereby lowering the thermal potential available for heat transfer. Under this condition, it is likely that the porous shell will attain its equilibrium state much sooner. Thus, it suggests that if Φ_κ is large enough, one need not be concerned with the transport in the porous zone because the interfacial temperature is more or less constant along the fluid surface.

The local Nusselt number, the interfacial temperature, and the interfacial velocity are presented in Figs. 6–8, respectively. As discussed before, the Prandtl number does not exhibit any profound impact, even in a localized fashion according to Figs 6(b), 7b(b) and 8(b). On the contrary, both Ra and Da play a controlling role on the shape of the interfacial profiles. However, in order for Da to have any substantial influence, it has to be greater than 10^{-5} or else the effects are quite minimal. As for the thermal con-

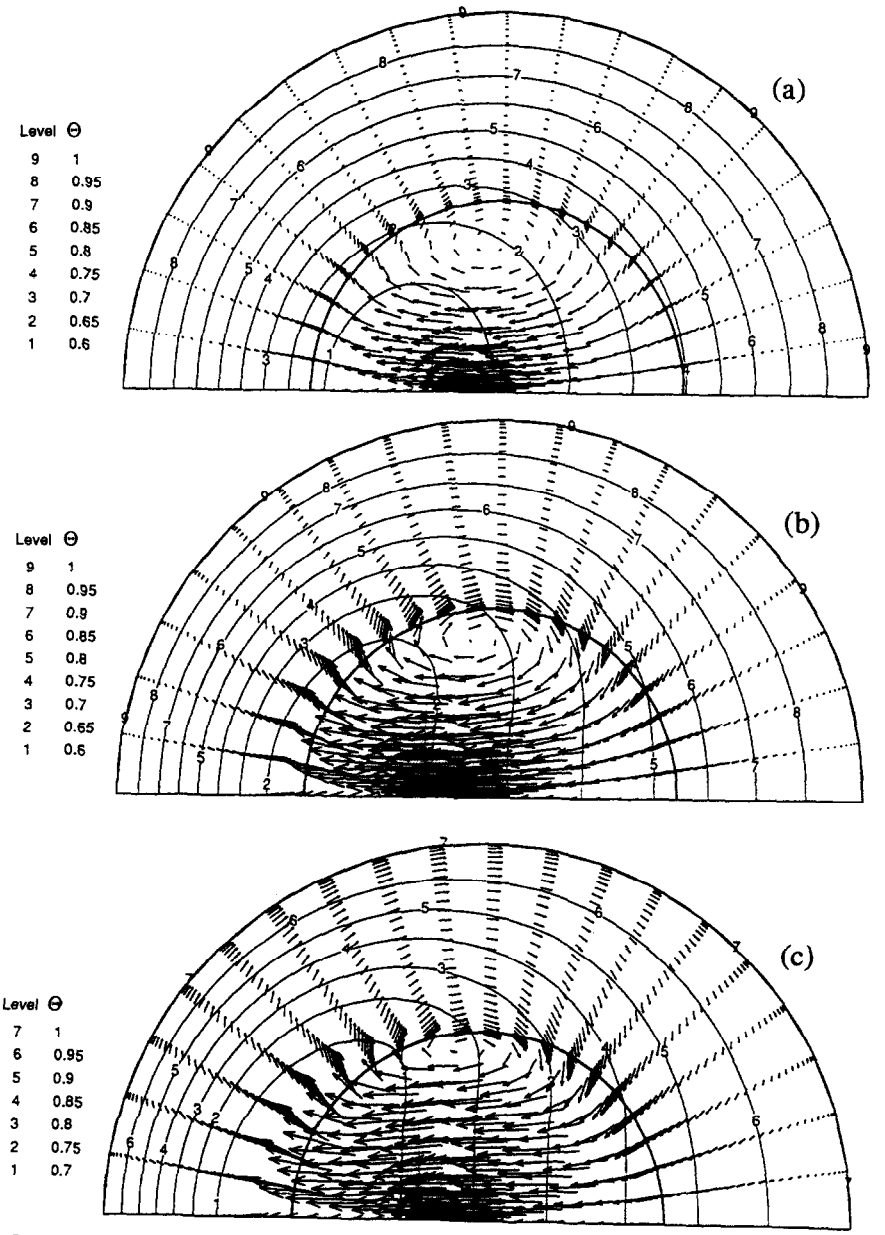

Fig. 4. Velocity and temperature fields at $t = 0.2$ for $Da = 10^{-5}$, $Pr = 3$ and $\Phi_\kappa = 0.7$: (a) $Ra = 10^4$; (b) $Ra = 10^5$; (c) $Ra = 10^6$.

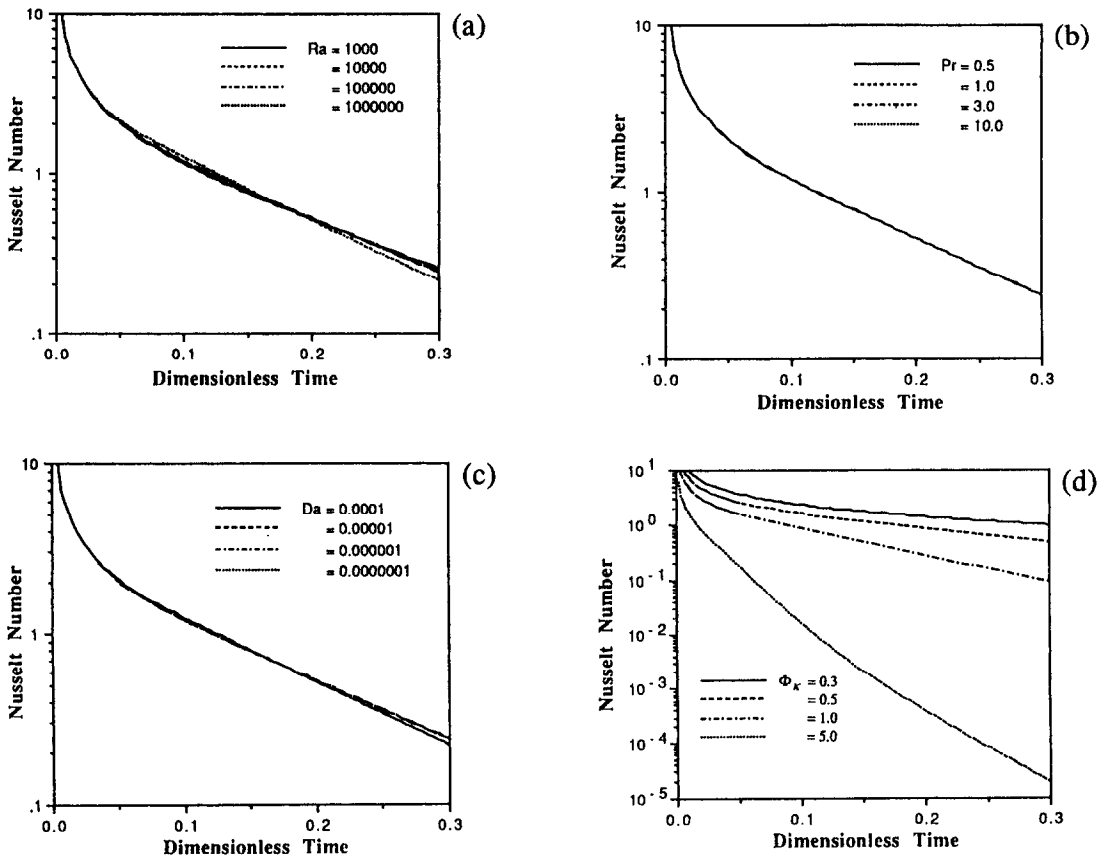

Fig. 5. Instantaneous average Nusselt number: (a) *Ra* varying; (b) *Pr* varying; (c) *Da* varying; (d) Φ_κ varying.

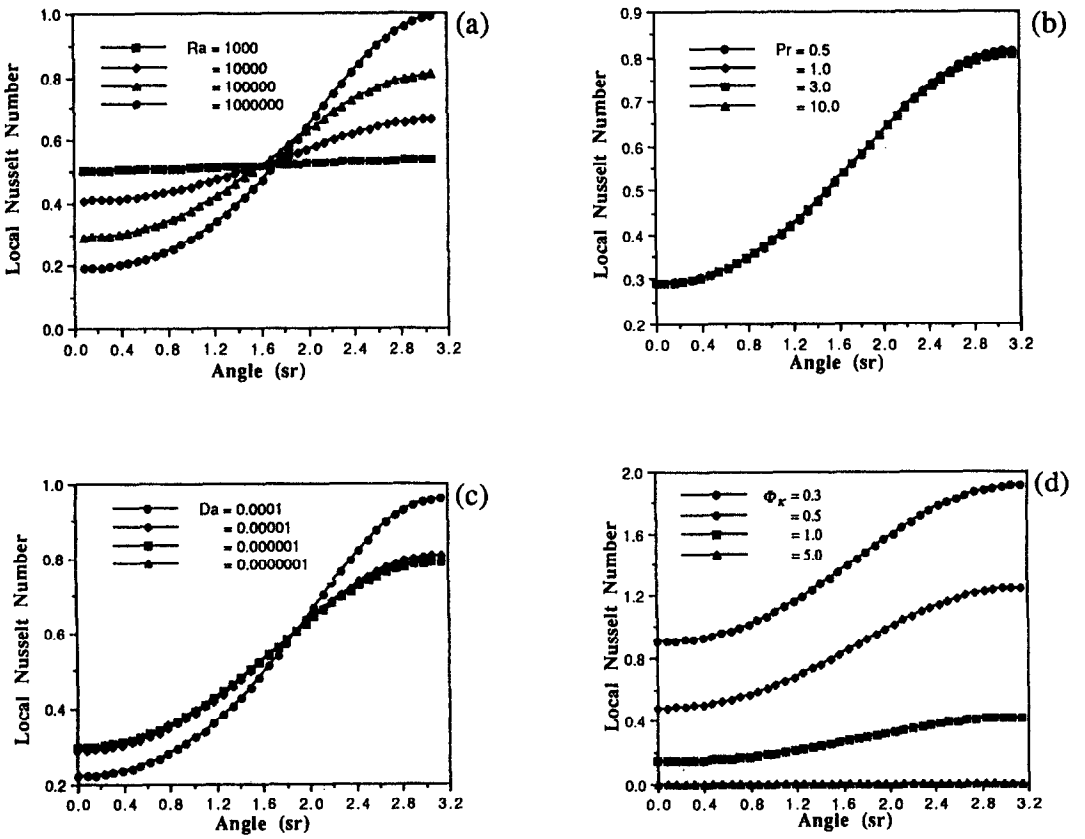

Fig. 6. Local Nusselt number at $t = 0.2$: (a) *Ra* varying; (b) *Pr* varying; (c) *Da* varying; (d) Φ_K varying.

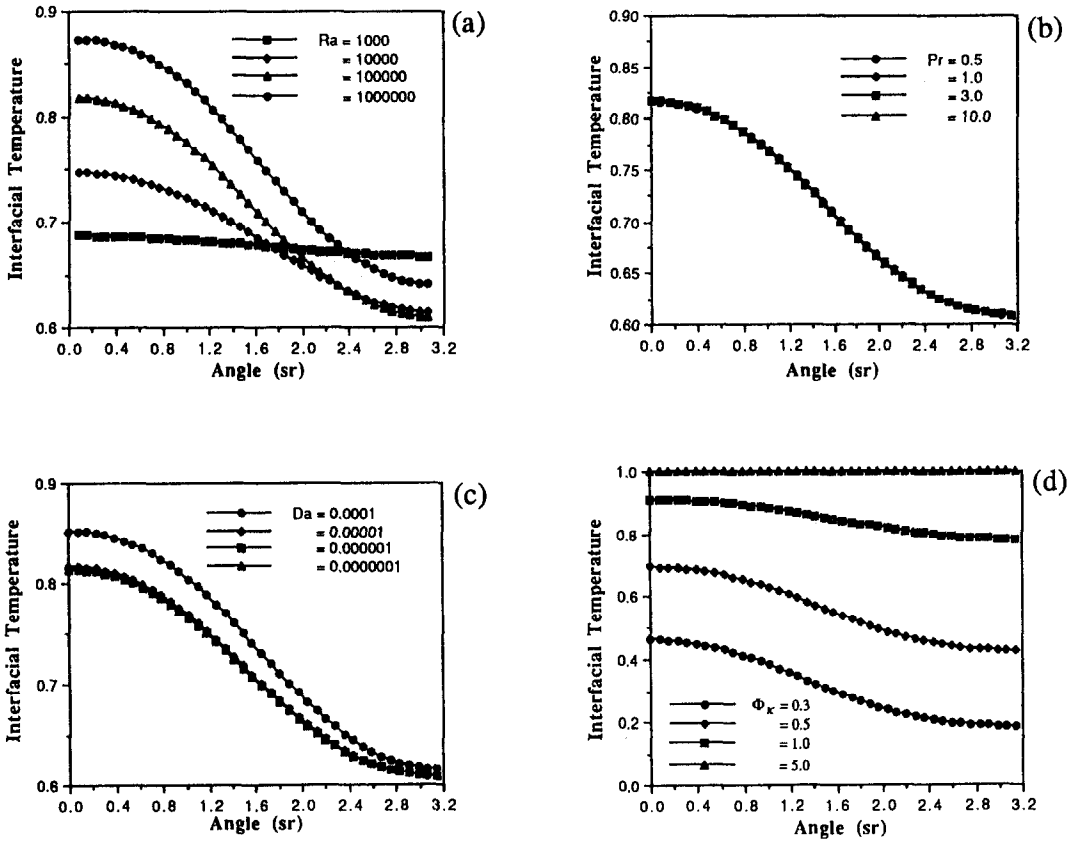

Fig. 7. Interfacial temperature at $t = 0.2$: (a) *Ra* varying; (b) *Pr* varying; (c) *Da* varying; (d) Φ_K varying.

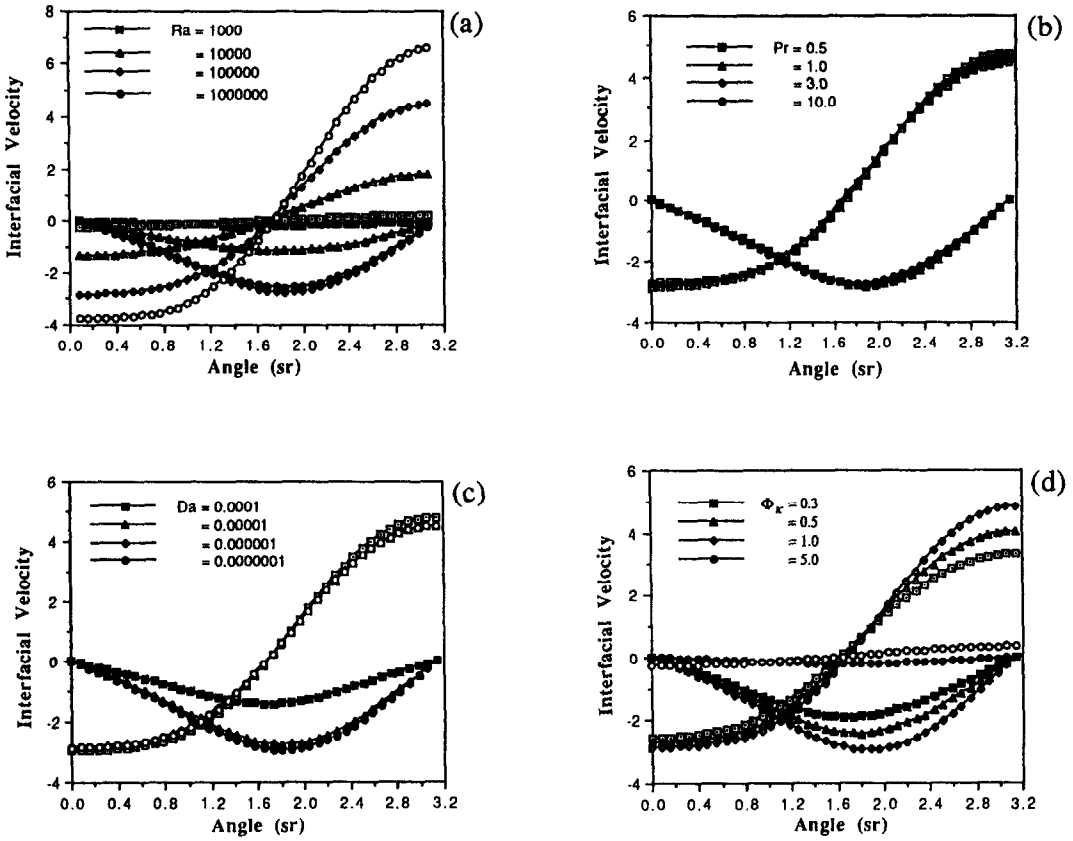

Fig. 8. Interfacial velocity at $t = 0.2$: (a) *Ra* varying; (b) *Pr* varying; (c) *Da* varying; (d) Φ_K varying.

ductivity ratio Φ_K, a change of value simply shifts the entire profile up or down depending on whether the change is an increase or a decrease. This characteristic is especially true for the local Nusselt number and the interfacial temperature. For the interfacial velocity, effects of Φ_K are far more pronounced in the back than in the front.

5. CONCLUDING REMARKS

A parametric study has been performed to investigate the transport in a spherical enclosure containing simultaneous fluid and porous layers. Based on the numerical results, it is concluded that

(1) The velocity inside the fluid core is dictated by both the induced temperature gradients, as well as in the interfacial momentum flux.

(2) The overall heat transfer rate is primarily controlled by the transport characteristic in the porous region and the thermal conductivity ratio of the inside to the outside.

(3) The Rayleigh number provides a measure of the convection effects on the heat transfer rate which may differ by as much as 20% for *Ra* in the range from 10^3 to 10^6. In addition, it causes a slight displacement of the vortex center.

(4) The Darcy number seems to alter the interfacial profiles only if $Da > 10^{-5}$. However, the deviations in the average Nusselt number are likely to be less than 10% for $10^{-7} < Da < 10^{-3}$.

Acknowledgements—The authors are grateful to Dr Rod Douglass of EG&G Idaho, Inc. for his critical reading the manuscript. This work is performed under the auspices of the U.S. Department of Energy, contract DE-AC07-76-ID01570, and is supported in part by the INEL Long-Term Research Initiative in Computational Mechanics.

REFERENCES

1. D. A. Nield, Onset of convection in a fluid layer overlying a layer of a porous medium, *J. Fluid Mech.* **81**, 513–522 (1977).
2. T. Nishimura, T. Takumi, M. Shiraishi, Y. Kawamura and H. Ozoe, Numerical analysis of natural convection in a rectangular enclosure horizontally divided into fluid and porous region, *Int. J. Heat Mass Transfer* **29**, 889–898 (1986).
3. T. W. Tong and E. Subramanian, Natural convection in rectangular enclosures partially filled with a porous medium, *Int. J. Heat Fluid Flow* **7**, 3–10 (1986).
4. S. B. Sathe, W.-Q. Lin and T. W. Tong, Natural convection in enclosures containing an insulation with a permeable fluid–porous interface, *Int. J. Heat Fluid* **9**, 389–395 (1988).
5. S. B. Sathe and T. W. Tong, Experimental study of natural convection in a partially porous enclosure, *J. Thermophys. Heat Transfer* **1**, 260–267 (1987).
6. C. Beckermann, S. Ramadhyani and R. Viskanta, Natural convection flow and heat transfer between a fluid

layer and a porous layer inside a rectangular enclosure, *J. Heat Transfer* **109,** 363–370 (1987).
7. C. Beckermann, R. Viskanta and S. Ramadhyani, Natural convection in vertical enclosures containing simultaneously fluid and porous layer, *J. Fluid Mech.* **186,** 257–284 (1988).
8. V. R. Voller, A. D. Brent and C. Prakash, The modeling of heat, mass and solute transport in solidification systems, *Int. J. Heat Mass Transfer* **32,** 1719–1731 (1989).
9. F. Shen, J. M. Khodadadi and Y. Zhang, Pseudosteady-state natural convection inside spherical containers, *ASME/JSME Thermal Engineering Conference*, Vol. 1, 209–216 (1995).
10. D. L. R. Oliver and J. N. Chung, Flow about a fluid sphere at low to moderate Reynolds numbers, *J. Fluid Mech.* **177,** 1–18 (1987).
11. H. D. Nguyen and J. N. Chung, A Chebyshev–Legendre spectal method for the transient solution of flow past a solid sphere, *J. Comput. Phys.* **104,** 303–312 (1993).
12. B. Abramzon and I. Borde, Conjugate unsteady heat transfer from a droplet in creeping flow, *A.I.Ch.E. J.* **26,** 536–544 (1980).
13. M. Rottenberg, R. Bivins, N. Metropolis and J. K. Wooten, *The 3-J and 6-J Symbols*. MIT Press, Cambridge, MA (1959).

APPENDIX

The followings are the convective terms which have been short-handed in equations (23)–(26)

$$S_n(X_1, X_2, \psi, \Theta) = \frac{1}{Pr\Delta t}\left[\frac{-1}{n(n+1)}\frac{d^2\psi_n^m}{dr^2} + \frac{\psi_n^m}{r^2}\right] + \frac{3}{2}NS(X_2, \psi^m, \Theta^m) - \frac{1}{2}NS(X_2, \psi^{m-1}, \Theta^{m-1}), \quad (A1)$$

$$H_n(\Phi_c, \Phi_\kappa, \psi, \Theta) = -\frac{\Phi_c}{\Phi_\kappa \Delta t}\Theta_n^m + \frac{3}{2}NH(\Phi_\kappa, \psi^m, \Theta^m) - \frac{1}{2}NH(\Phi_\kappa, \psi^{m-1}, \Theta^{m-1}), \quad (A2)$$

$$NS(X_2, \psi, \Theta) = -Ra\sum_{i=0}^{NL}\left\{\omega_{i1}^n\left(\frac{d\Theta_i}{dr} - \frac{\Theta_i}{r}\right) - \omega_{1i}^n\frac{\Theta_i}{r}\right\} + \frac{X_2}{Pr}\sum_{i=1}^{NL}\sum_{j=1}^{NL}\chi_{ij}^n\frac{d\psi_i}{dr}\left\{\frac{1}{j(j+1)r^2}\frac{d^2\psi_j}{dr^2} - \frac{\psi_j}{r^4}\right\} + \frac{X_2}{Pr}\sum_{i=1}^{NL}\sum_{j=1}^{NL}\omega_{ij}^n\psi_i\left\{\frac{1}{j(j+1)}\left[\frac{1}{r^2}\frac{d^3\psi_j}{dr^3} - \frac{2}{r^3}\frac{d^2\psi_j}{dr^2}\right] - \frac{1}{r^4}\frac{d\psi_j}{dr} + \frac{4}{r^5}\psi_j\right\}, \quad (A3)$$

$$NH(\Phi_\kappa, \psi, \Theta) = \frac{1}{r^2\Phi_\kappa}\sum_{i=0}^{NL}\sum_{j=1}^{NL} \times\left\{\gamma_{ij}^n\Theta_i\frac{d\psi_j}{dr} + \lambda_{ij}^n\left(\frac{d\Theta_i}{dr} - \frac{\Theta_i}{r}\right)\psi_j\right\}, \quad (A4)$$

with the coefficients ω_{ij}^n, χ_{ij}^n, λ_{ij}^n and γ_{ij}^n representing the integrals of products of Legendre and its associated functions. In terms of '3-J' symbols [13], they can be expressed as

$$\omega_{ij}^n = -(2n+1)\left[\frac{j(j+1)}{n(n+1)}\right]^{1/2}\begin{pmatrix} n & i & j \\ -1 & 0 & 1\end{pmatrix}\begin{pmatrix} n & i & j \\ 0 & 0 & 0\end{pmatrix} \quad (A5)$$

$$\chi_{ij}^n = (2n+1)\left[\frac{j(j^2-1)(j+2)}{n(n+1)i(i+1)}\right]^{1/2}\begin{pmatrix} n & i & j \\ -1 & -1 & 2\end{pmatrix} \times\begin{pmatrix} n & i & j \\ 0 & 0 & 0\end{pmatrix} \quad (A6)$$

$$\lambda_{ij}^n = \frac{2n+1}{2}\begin{pmatrix} n & i & j \\ 0 & 0 & 0\end{pmatrix}\begin{pmatrix} n & i & j \\ 0 & 0 & 0\end{pmatrix} \quad (A7)$$

$$\gamma_{ij}^n = \frac{-(2n+1)}{2}\left[\frac{j(j+1)}{i(i+1)}\right]^{1/2}\begin{pmatrix} n & i & j \\ 0 & 1 & -1\end{pmatrix}\begin{pmatrix} n & i & j \\ 0 & 0 & 0\end{pmatrix}. \quad (A8)$$